

Nanoscale Rigidity in Cross-Linked Micelle Networks Revealed by XPCS Nanorheology

M. Reiser,^{1,2,*} J. Hallmann,¹ J. Möller,¹ K. Kazarian,¹ D. Orsi,³ L. Randolph,² H. Rahmann,² F. Westermeier,⁴ E. Stellamanns,⁴ M. Sprung,⁴ F. Zontone,⁵ L. Cristofolini,³ C. Gutt,² and A. Madsen¹

¹European XFEL, Holzkoppel 4, 22869 Schenefeld, Germany

²Department Physik, Universität Siegen, Walter-Flex-Straße 3, 57072 Siegen, Germany

³Department of Mathematical, Physical and Computer Sciences,

University of Parma, Parco Area Scienze 7/A, 43124 Parma, Italy

⁴Deutsches Elektronen-Synchrotron, Notkestraße 85, 22607 Hamburg, Germany

⁵European Synchrotron Radiation Facility, 71, avenue des Martyrs, 38043 Grenoble, France

Solutions of wormlike micelles can form cross-linked networks on microscopic length scales. The unique mechanical properties of these complex fluids are driven by the interplay between the network structure and dynamics which are investigated by plate-plate rheometry and X-ray photon correlation spectroscopy (XPCS) nanorheology. Intensity auto-correlation functions of tracer nanoparticles (NPs) dispersed in micelle solutions were recorded which captured both the slow structural network relaxation and the short-time dynamics of NPs trapped in the network. The results are indicative of a resonance-like dynamic behavior of the network on the nanoscale that develops as a consequence of the intrinsic short-range rigidity of individual micelle chains.

Complex networks formed by long cylindrical or wormlike molecules are ubiquitous in nature and technology. Prominent examples are for instance hydrogels and the cytoskeleton. These complex networks are mainly functionalized by non-linear viscoelastic properties where, *e.g.* in the cytoskeleton [1, 2], networks built up from microscopic filaments determine intracellular transport, mobility and stabilization [3–5] and shear induced strain-stiffening preserves the network shape under external stresses [6].

Different phenomena have been discussed in terms of their contributions to non-linear elasticity in complex networks, *e.g.* connectivity [7, 8], bending and stretching forces [9], cross-link density [10], cross-link dynamics and polydispersity [11]. Many of these phenomena are depending on the interplay between the nanoscale network structure and dynamics where systematic investigations are challenging for both theory and experiments.

A prominent example of such nanoscale cross-linked network systems are wormlike micelles [12, 13]. Above a critical concentration, surfactant molecules self-assemble to form micelles. The micellar shape is determined by properties of the surfactant molecule and in particular by the ratio of the volumes of its hydrophobic and hydrophilic parts. Wormlike micelles are promising candidates in the pursue of new “smart” materials that change their function and structure in response to external stimuli (electrical, optical, thermal, etc.) [14–16].

Ketner *et al.* [17] discovered that aqueous solutions of cetyl trimethylammonium bromide (CTAB) [12, 18] and orthomethoxycinnamic acid (OMCA) [19, 20] exhibit remarkable viscoelastic properties due to the self-assembly of long ($\approx 300\text{nm}$) wormlike micelles that form a cross-linked or branched network. A characteristic length scale of the network is ξ , the hydrodynamic correlation length or network mesh size (Fig. 1). Although wormlike micelles can be described as flexible chains they possess short-range rigidity described by the *Kuhn-length*, b [21], which is a measure of the chain link dimension (Fig. 1).

Experimentally it is challenging to investigate dynamics

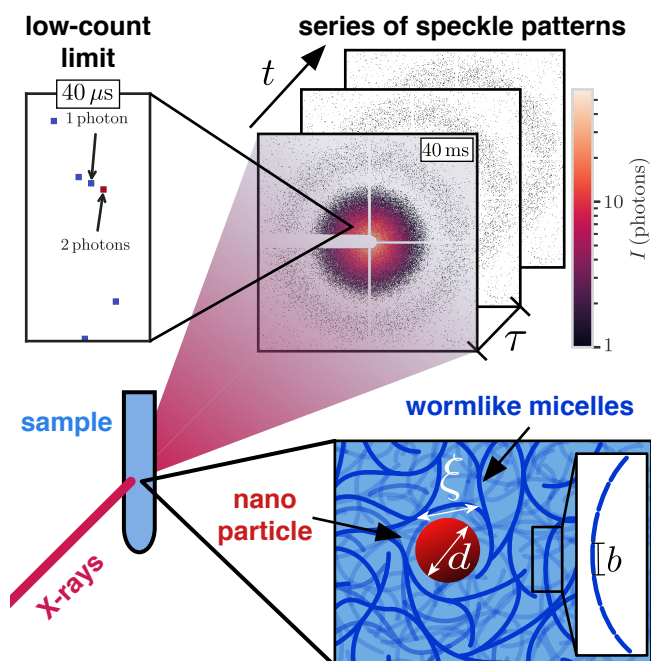


Figure 1. Experimental schematics: Nanoparticles with a diameter of $d = 100\text{nm}$ are dispersed in the OMCA-CTAB solutions. The characteristic mesh size of the network is denoted ξ and b is the Kuhn-length. The sample is illuminated by partially coherent X-rays and series of speckle patterns are acquired by a 2D pixel detector in the far-field. Speckle series were recorded with different exposure times down to the limit of a few photons per frame.

on the length scale of individual chains. Nanorheological techniques hold promise to gain insight into local phenomena in complex fluids by measuring the dynamics of nanoparticles (NPs) dispersed as tracers in the solutions [22–24]. One possibility of obtaining dynamical information on the NP dynamics is photon correlation spectroscopy where the tracer dynamics are deduced from speckle fluctuations—interference fringes that occur in the far field when the sample is illuminated by (partially) coherent light. In order

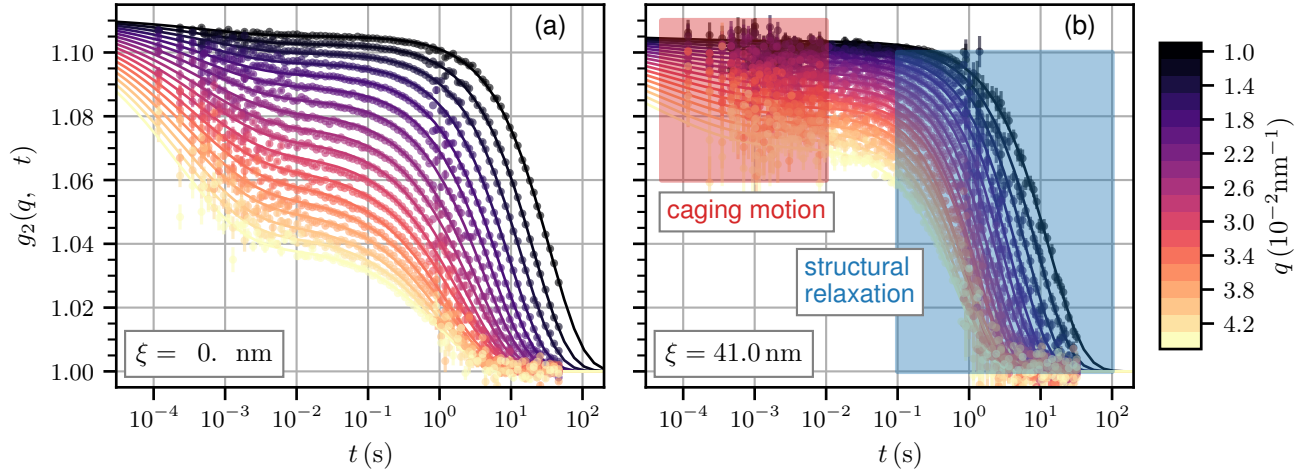


Figure 2. Intensity auto-correlation functions, $g_2(q, \Delta t)$, measured with 100 nm silica NPs dispersed in OMCA-CTAB solutions of 50 mM (a) and 80 mM (b) surfactant and acid concentration. The two relaxation modes are indicated in blue and red. Solid lines are fits with a double exponential model in Eq. (1).

to measure NP dynamics in dense micelle solutions, X-ray photon correlation spectroscopy (XPCS) [25–28] was performed (Fig. 1). XPCS allows investigation of length scale dependent dynamics on microscopic length scale due to the short X-ray wavelength. Novel X-ray detectors are capable of acquiring scattering images with several kilohertz repetition rate so the full dynamical spectrum from microseconds to hundreds of seconds is covered (Fig. 2).

OMCA-CTAB samples were prepared according to the recipe of Ketner *et al.* [17] with surfactant concentrations ranging from 20 mM to 200 mM. The OMCA concentration was equal to the CTAB concentration for all solutions. Aqueous solutions of OMCA and CTAB were prepared in separate beakers. When combining the solutions, the viscosity instantaneously increases due to the formation of the branched wormlike micelle network. Spherical silica NPs with a diameter of $d = 100$ nm were used as tracers. The NP volume fraction (0.04 %) was tuned to optimize the scattering signal while reducing possible effects on the micelle formation to a minimum. The solutions were filled into quartz capillaries with an outer diameter of 2 mm for the XPCS measurements.

XPCS experiments were conducted at P10 at PETRA III (DESY) and ID10 (ESRF) employing partially coherent X-rays with a photon energy of 8.1 keV. A Si (111) monochromator reduced the bandwidth to $\Delta E/E \approx 10^{-4}$ to increase the longitudinal coherence. The experiments at ID10 were conducted with a beam size of 10 μ m and a sample-detector distance of 5.1 m. At P10 the beam size was increased to 75 μ m in favor of a lower radiation dose. In this case the sample-detector distance must be increased to have an adequate speckle contrast and 20 m was used. Two-time correlation functions were employed to identify the onset of radiation damage yielding a dose threshold of 2 kGy which corresponds to less than one second illumination by the unattenuated beam. Consequently, for every measurement data

were acquired until this dose was reached. Afterwards, the beam position on the sample was changed for the next acquisition. Attenuating the beam allowed for including longer time scales. Thereby, the correlation functions could be measured step-wise and stitched together covering time scales from microseconds to tens of seconds (Fig. 2).

The correlation functions exhibit a two-step relaxation process indicative of the structural network dynamics on long time scales and the localized caging motion of trapped NPs on short time scales. Hence, the correlation functions can be modeled by the sum of two exponential modes:

$$g_2(q, \Delta t) = 1 + \beta_0 \sum_{i=1}^2 \beta_i(q) \exp \left\{ -2 (\Gamma_i(q) \Delta t)^{\alpha_i(q)} \right\}, \quad (1)$$

where β_0 is the speckle contrast, β_i are the relative strengths ($\beta_1 = 1 - \beta_2$), Γ_i are the relaxation rates, and α_i are the Kohlrausch-Williams-Watts (KWW) exponents. The indices 1 and 2 are referring to the short- and long-time relaxation, respectively (Fig. 2).

The localization length, r_{loc} , of the NPs is calculated by fitting the relative strength (non-ergodicity level) as a function of q with $\beta_2 = \exp(-r_{loc}^2 q^2 / 3)$ [27]. r_{loc} is related to the hydrodynamic correlation length or network mesh size, ξ , by [29]

$$\xi^3 = r_{loc}^2 d = k_B T / G_0. \quad (2)$$

This allows comparing XPCS and classical rheology where ξ is inferred from the plateau modulus G_0 . k_B is the Boltzmann constant and T the temperature.

Rheology measurements were conducted with a HAAKE MARS III rheometer at DESY and G_0 was obtained from the complex moduli by fitting a Maxwell model. The resulting ξ values calculated using Eq. (2) are displayed in Fig. 3 as a function of concentration, c . Several correlation functions were measured with each concentration (~ 5 per

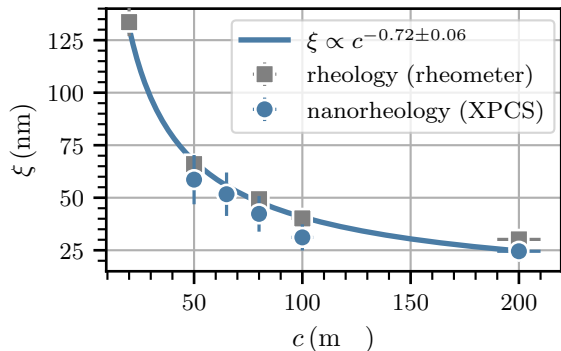


Figure 3. Hydrodynamic correlation length, ξ , determined by XPCS based nanorheology and classical rheology with a plate-plate rheometer (see Eq. (2)). The solid line indicates a power law fit.

concentration). The errorbars in Fig. 3 reflect the standard deviation of ξ for different samples with the same concentration. The error of an individual XPCS measurement is: $\delta\xi \lesssim 2\text{nm}$. Apparently, the characteristic network length scales determined by both methods (XPCS and rheology) are in agreement. A power law fit results in a scaling exponent of -0.72 ± 0.06 as expected for a network of semi-flexible wormlike micelles [30].

Information about the dynamics is encoded in the dispersion relations, $\Gamma_i(q)$, obtained from fits of the correlation functions. Fig. 4 displays the relaxation rates obtained from the data in Fig. 2(a). The slow structural relaxation (blue) is well modeled by a power law of the form $\Gamma_2(q) = D_2 q^{n_2}$ whereas the short-time dispersion relation, $\Gamma_1(q)$ (red), can be described by

$$\Gamma_1(q) = D_1 q^{n_1} + \Gamma_0. \quad (3)$$

Here, D_i are generalized diffusion coefficients and n_i the corresponding scaling exponents of both relaxation processes. Interestingly, $\Gamma_1(q)$ exhibits a clear plateau, $\Gamma_0 > 0$, for small momentum transfers which is characteristic of confined dynamics [31].

Correlation functions of different q -bins are fitted simultaneously with Eq. (1) to (3) to determine the dynamical parameters. The reader is referred to the SI for a detailed description of the data treatment. Fig. 4 displays histograms of the q -scaling exponents, n_i , over the acquired datasets. The mean values of the corresponding distributions reflect the different nature of the two relaxation processes. While the structural relaxation (blue) exhibits close to diffusive behavior ($n_2 = 2$), the short-time caging motion is found to be subdiffusive with $n_1 \approx 3.9$. This subdiffusivity originates from restricted motion of NPs inside transient network cages and is hence another evidence for confinement. The KWW exponents, α_1 (not shown), support the same picture with $\alpha_1 \approx 0.5$ for the short-time dynamics meaning that the correlation functions resemble stretched exponential decays.

When a NP is trapped inside a network cage, its dynamics are strongly influenced by interactions with the micelles

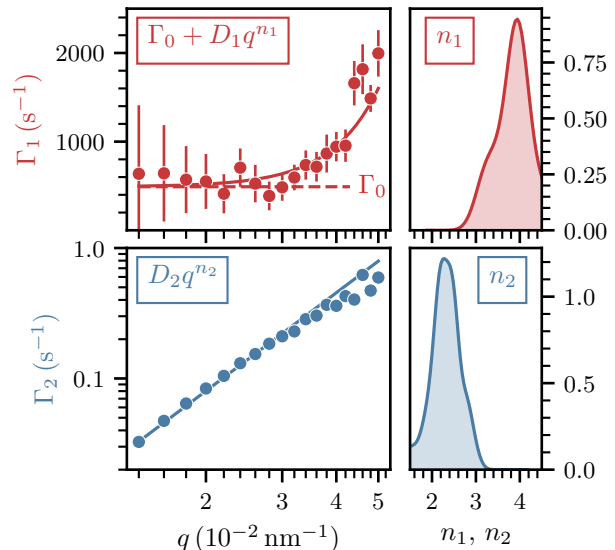


Figure 4. (left panels) Dispersion relations of the localized caging motion and the structural network relaxation are plotted in red and blue, respectively. The data are deduced from the correlation function in Fig.2(a). The functional forms of the dispersion relations are indicated on the figures. (right panels) Distributions of the exponents, n_i , over all data sets of correlation functions (in total 25).

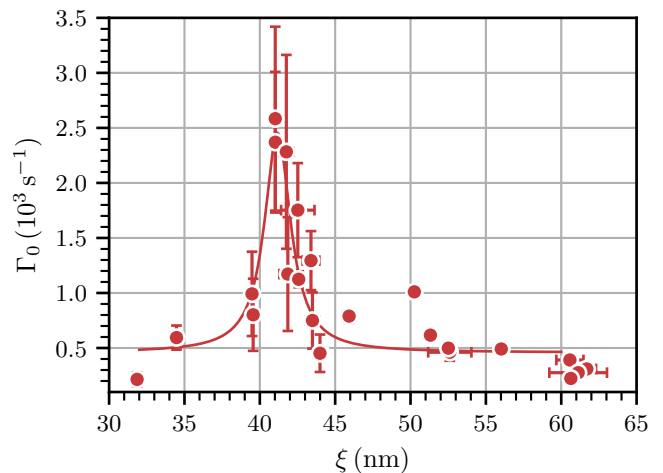


Figure 5. The slowest relaxation time under confinement, Γ_0 (plateau value), plotted versus the mesh size, ξ (points). The resonance peak of maximum network stiffness is modeled by a Lorentzian function plus a constant background (solid line). The peak position is $\xi_0 = (41.2 \pm 0.2)\text{nm}$.

defining the cage boundaries. Therefore, microscopic network properties on length scales on the order of the cage size are related to the short-time NP dynamics which is characterized by the parameter Γ_0 introduced in Eq. (3). Γ_0 is the slowest relaxation rate of the tracers before they escape confinement (structural relaxation) and is hence a measure for the network stiffness on nanometer length scale. Γ_0 exhibits a resonance-like maximum as a function of ξ shown in Fig. 5. The narrow peak occurs at a mesh size of

$\xi_0 = (41.2 \pm 0.2)$ nm with a full width at half maximum of (2.1 ± 0.5) nm (fitted by a Lorentzian function plus a constant background of $(0.46 \pm 0.08) \times 10^3 \text{ s}^{-1}$). This behavior indicates that the OMCA-CTAB network develops enhanced stiffness resulting in a strong repulsive force on the NPs leading to an increased relaxation rate. The peak of Γ_0 occurs at a hydrodynamic correlation length, ξ , close to the Kuhn length, b , found for wormlike CTAB micelles [21]. b is the length scale that describes the intrinsic micelle rigidity. Conclusively, the microscopic network stiffness is determined by the short-range rigidity of individual micelle strands. Furthermore, the observed maximum of Γ_0 shows that the stiffness is non-linearly increasing when the network mesh size is matching the Kuhn-length of the micelles, similar to a resonance effect.

The dynamical behavior of the OMCA-CTAB micelle network resembles previously observed phenomena in branched fiber networks displaying non-linear mechanical response to deformation [6, 7, 9, 11]. Under a certain critical strain, those cross-linked fiber networks undergo a soft-to-rigid phase transition accompanied by increased susceptibility of dynamical properties like differential non-affinity [9] or the changing rate of the bending angle [8]. However, those processes are mostly studied on macroscopic scale using standard rheometry techniques. Obviously, for understanding fundamental processes in cross-linked networks and designing new functional nanocomposites, the coupling of the structural and dynamical network properties has to be studied locally. We have shown here that nanorheology XPCS is ideally suited to obtain this information. The XPCS data reveal a connection between the micelle rigidity and the hydrodynamic network properties in the OMCA-CTAB system on the nanoscale. The low dose XPCS experiments presented here pave the way for investigations of general complex networks by studying the interplay between nanoscale structure and dynamics.

We acknowledge the support from the beam line staff at ID10 and P10 during the preparation of the experiments and the beamtimes. CG acknowledges support from BMBF via projects 05K19PS1 and Röntgen-Ångström Cluster Grant 05K20PSA.

* mario.reiser@xfel.eu

- [1] R. H. Pritchard, Y. Y. Shery Huang, and E. M. Terentjev, Mechanics of biological networks: From the cell cytoskeleton to connective tissue, *Soft Matter* **10**, 1864 (2014).
- [2] D. A. Fletcher and R. D. Mullins, Cell mechanics and the cytoskeleton, *Nature* **463**, 485 (2010).
- [3] M. Otten, A. Nandi, D. Arcizet, M. Gorelashvili, B. Lindner, and D. Heinrich, Local Motion Analysis Reveals Impact of the Dynamic Cytoskeleton on Intracellular Subdiffusion, *Biophysical Journal* **102**, 758 (2012).
- [4] P. K. Mattila and P. Lappalainen, Filopodia: Molecular architecture and cellular functions, *Nat. Rev. Mol. Cell Biol.* **9**, 446 (2008).
- [5] M. L. Gardel, K. E. Kasza, C. P. Brangwynne, J. Liu, and D. A. Weitz, Chapter 19 Mechanical Response of Cytoskeletal Networks, in *Methods in Cell Biology*, Vol. 89 (Elsevier, 2008) pp. 487–519.
- [6] K. A. Jansen, A. J. Licup, A. Sharma, R. Rens, F. C. MacKintosh, and G. H. Koenderink, The Role of Network Architecture in Collagen Mechanics, *Biophysical Journal* **114**, 2665 (2018).
- [7] A. Sharma, A. J. Licup, K. A. Jansen, R. Rens, M. Sheinman, G. H. Koenderink, and F. C. MacKintosh, Strain-controlled criticality governs the nonlinear mechanics of fibre networks, *Nature Phys* **12**, 584 (2016).
- [8] A. Sharma, A. J. Licup, R. Rens, M. Vahabi, K. A. Jansen, G. H. Koenderink, and F. C. MacKintosh, Strain-driven criticality underlies nonlinear mechanics of fibrous networks, *Phys. Rev. E* **94**, 042407 (2016).
- [9] R. Rens, M. Vahabi, A. J. Licup, F. C. MacKintosh, and A. Sharma, Nonlinear Mechanics of Athermal Branched Biopolymer Networks, *J. Phys. Chem. B* **120**, 5831 (2016).
- [10] M. L. Gardel, Elastic Behavior of Cross-Linked and Bundled Actin Networks, *Science* **304**, 1301 (2004).
- [11] F. Meng and E. M. Terentjev, Fluidization of Transient Filament Networks, *Macromolecules* **51**, 4660 (2018).
- [12] M. E. Cates and S. J. Candau, Statics and dynamics of wormlike surfactant micelles, *J. Phys.: Condens. Matter* **2**, 6869 (1990).
- [13] C. A. Dreiss, Wormlike micelles: Where do we stand? Recent developments, linear rheology and scattering techniques, *Soft Matter* **3**, 956 (2007).
- [14] S. Matsumoto, S. Yamaguchi, S. Ueno, H. Komatsu, M. Ikeda, K. Ishizuka, Y. Iko, K. V. Tabata, H. Aoki, S. Ito, H. Noji, and I. Hamachi, Photo Gel-Sol/Sol-Gel Transition and Its Patterning of a Supramolecular Hydrogel as Stimuli-Responsive Biomaterials, *Chem. - Eur. J.* **14**, 3977 (2008).
- [15] Z. Chu, C. A. Dreiss, and Y. Feng, Smart wormlike micelles, *Chem. Soc. Rev.* **42**, 7174 (2013).
- [16] Y. Feng, Z. Chu, and C. A. Dreiss, *Smart Wormlike Micelles*, SpringerBriefs in Molecular Science (Springer Berlin Heidelberg, Berlin, Heidelberg, 2015).
- [17] A. M. Ketner, R. Kumar, T. S. Davies, P. W. Elder, and S. R. Raghavan, A Simple Class of Photorheological Fluids: Surfactant Solutions with Viscosity Tunable by Light, *J. Am. Chem. Soc.* **129**, 1553 (2007).
- [18] J. Tao, H.-y. Yang, X. Hao, Y.-j. Xie, and H.-y. Li, Effect of ortho-methoxycinnamic acid on the sol-gel transition of methylcellulose solutions in the presence of cetyltrimethylammonium bromide, *Chin. J. Polym. Sci.* **31**, 263 (2013).
- [19] M. D. Cohen, The Photochemistry of Organic Solids, *Angew. Chem. Int. Ed. Engl.* **14**, 386 (1975).
- [20] S. D. M. Atkinson, M. J. Almond, S. J. Hibble, P. Hollins, S. L. Jenkins, M. J. Tobin, and K. S. Wiltshire, An in situ time-dependent study of the photodimerisation of chloro-derivatives of trans-cinnamic acid using infrared microspectroscopy with a synchrotron radiation source, *Phys. Chem. Chem. Phys.* **6**, 4 (2004).
- [21] W.-R. Chen, P. D. Butler, and L. J. Magid, Incorporating Intermolecular Interactions in the Fitting of SANS Data from Cationic Wormlike Micelles, *Langmuir* **22**, 6539 (2006).
- [22] M. L. Gardel, M. T. Valentine, J. C. Crocker, A. R. Bausch, and D. A. Weitz, Microrheology of Entangled F-Actin Solutions, *Phys. Rev. Lett.* **91**, 10.1103/PhysRevLett.91.158302 (2003).
- [23] T. G. Mason and D. A. Weitz, Optical Measurements of Frequency-Dependent Linear Viscoelastic Moduli of Complex Fluids, *Phys. Rev. Lett.* **74**, 1250 (1995).
- [24] H. Guo, G. Bourret, R. B. Lennox, M. Sutton, J. L. Harden, and R. L. Leheny, Entanglement-Controlled Subdiffusion of

- Nanoparticles within Concentrated Polymer Solutions, *Phys. Rev. Lett.* **109**, 10.1103/PhysRevLett.109.055901 (2012).
- [25] G. Grübel and F. Zontone, Correlation spectroscopy with coherent X-rays, *J. Alloys Compd.* **362**, 3 (2004).
- [26] C. Gutt, L.-M. Stadler, A. Duri, T. Autenrieth, O. Leupold, Y. Chushkin, and G. Grübel, Measuring temporal speckle correlations at ultrafast x-ray sources, *Opt. Express* **17**, 55 (2009).
- [27] R. L. Leheny, XPCS: Nanoscale motion and rheology, *Curr. Opin. Colloid Interface Sci.* **17**, 3 (2012).
- [28] A. Madsen, A. Fluerasu, and B. Ruta, Structural Dynamics of Materials Probed by X-Ray Photon Correlation Spectroscopy, in *Synchrotron Light Sources and Free-Electron Lasers* (Springer International Publishing, Cham, 2016) pp. 1617–1641.
- [29] L.-H. Cai, S. Panyukov, and M. Rubinstein, Mobility of Non-sticky Nanoparticles in Polymer Liquids, *Macromolecules* **44**, 7853 (2011).
- [30] M. Cates, Dynamics of living polymers and flexible surfactant micelles : Scaling laws for dilution, *J. Phys.* **49**, 1593 (1988).
- [31] M. Bée, *Quasielastic Neutron Scattering: Principles and Applications in Solid State Chemistry, Biology, and Materials Science* (Adam Hilger, Bristol, England ; Philadelphia, 1988).

SI: Nanoscale Rigidity in Cross-Linked Micelle Networks Revealed by XPCS Nanorheology

M. Reiser, et al.^{1,*}

¹European XFEL, Holzkoppel 4, 22869 Schenefeld, Germany

RHEOLOGY MEASUREMENTS

The viscoelastic nature of the OMCA-CTAB micelle solution is evident in the complex moduli (Fig. 1). The solid line shows a fit with the standard Maxwell model where the storage and loss modulus as a function of the shear frequency, ω , are given by

$$G'(\omega) = G_0 \frac{\tau_R^2 \omega^2}{1 + \omega^2 \tau_R^2} \quad \text{storage modulus,} \quad (1)$$

$$G''(\omega) = G_0 \frac{\tau_R \omega}{1 + \omega^2 \tau_R^2} \quad \text{loss modulus,} \quad (2)$$

τ_R is the terminal stress relaxation time and G_0 is the plateau modulus.

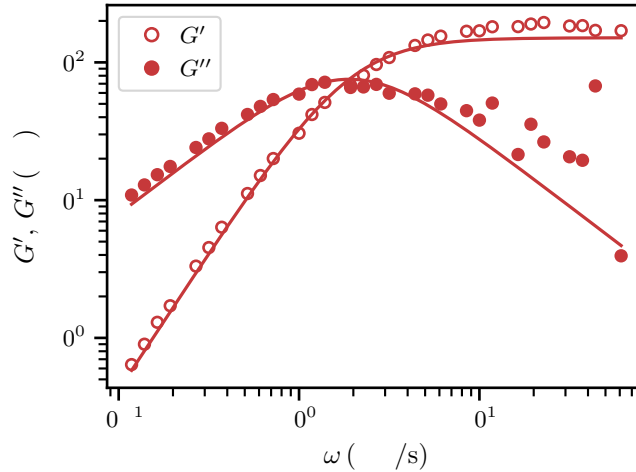


Figure 1. Complex moduli of a 200 mM OMCA-CTAB solution. The storage and loss modulus, G' , G'' , are fitted with the standard Maxwell model (solid lines).

XPCS MEASUREMENT PROTOCOL

The OMCA-CTAB system is very susceptible to radiation damage and a certain illuminated volume of the sample can only stand a limited radiation dose before the properties are altered by the X-rays. To study possible effects of the X-ray beam on the sample dynamics, time resolved correlation functions are calculated as a function of the absorbed dose, \mathcal{D} , during a measurement:

$$c_2(q, \mathcal{D}_1, \mathcal{D}_2) = \frac{\langle I(q, \mathcal{D}_1) I(q, \mathcal{D}_2) \rangle_p}{\langle I(q, \mathcal{D}_1) \rangle_p \langle I(q, \mathcal{D}_2) \rangle_p}. \quad (3)$$

Figure 2(b) displays $c_2(q, \mathcal{D}_1, \mathcal{D}_2)$ measured with 100 nm silica nanoparticles in a 50 mM OMCA-CTAB solution. Cuts parallel to the diagonal (marked in different shades of blue) are plotted as a function of the absorbed dose in Figure 2(a) and normalized to the initial contrast. After roughly 10 kGy, the contrast drops steeply indicating that the X-rays are damaging the micelle network resulting in an acceleration of the dynamics. To be on the safe side, a maximum dose of 2 kGy was chosen for the XPCS measurements.

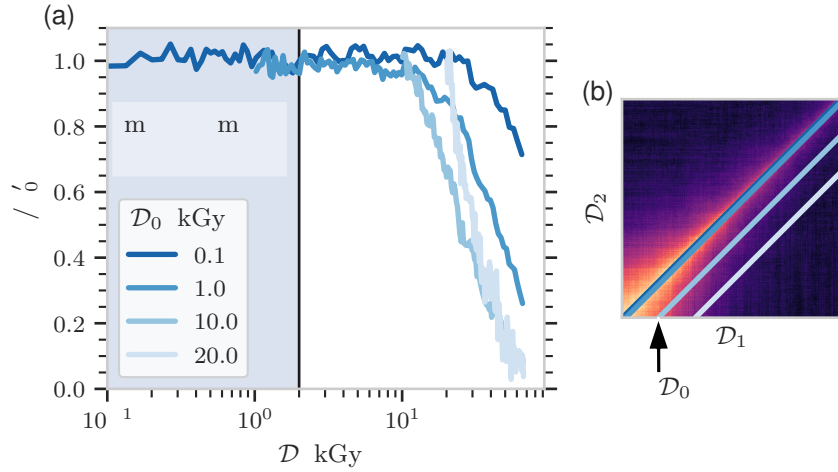


Figure 2. (a) The normalized contrast is extracted from diagonal cuts of the time resolved correlation function (b) as a function of the absorbed dose during a measurement, D_1 , D_2 . A measurement window up to 2 kGy is chosen to safely exclude beam damage effects in the XPCS measurements.

DETERMINATION OF DYNAMICAL PARAMETERS

Fig. 1 in the letter shows that for the shortest exposure time of 40 μ s the scattered intensity is reduced to less than 1×10^{-2} photons per pixel. This requires many repetitions to increase the signal-to-noise ratio of a set of correlation functions. For instance the correlation functions shown in Fig. 2 in the main text are calculated from ca. two million speckle patterns.

Additionally, a global fitting scheme was used for the parameter estimation. The dynamical parameters ξ , D_i , α_i , n_i and Γ_0 are calculated by globally fitting a dataset of correlation functions (all available q -bins) with the double exponential model for $g_2(q, t)$ introduced in the letter. The residuals are minimized by a Levenberg-Marquardt algorithm. The parameters describing the structural relaxation were considered as free fitting parameters. Let N_q be the number of q -bins, then the parameters of the structural relaxation are $\alpha_1^{N_q} \dots \alpha_2^{N_q}$ and $\Gamma_2^1 \dots \Gamma_2^{N_q}$. The exponent n_2 is determined by fitting $\Gamma_2(q) = D_2 q^{n_2}$. To fit the fast relaxation mode the q -dependence of the short-time dispersion relation is modeled by $\Gamma_1(q) = \Gamma_0 + D_1 q^{n_1}$ resulting in a reduced number of fit parameters. Consequently, Γ_0 , D_1 and n_1 are inferred directly from the correlation functions.

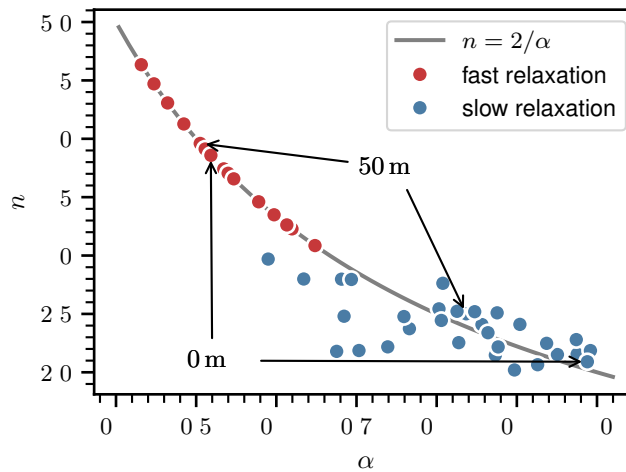


Figure 3. Correlation plot of the q -scaling exponent, n , and the KWW-exponent, α . The color distinguishes between the short- and long-time relaxation. The solid gray line indicates $n = 2/\alpha$. The data points corresponding to the correlation functions shown in the manuscript are annotated.

The parameters n_2 and the average α_2 are inversely proportional to each other as shown in Fig. 3 in blue. Their

relation can be described by

$$n_i = 2/\alpha_i, \quad (4)$$

as indicated by the gray line. In general, the two relaxation processes can only be resolved with sufficient time resolution and when they are well separated. In addition to the data shown in the main text where these conditions are fulfilled Fig. 3 contains additional datasets where the fast relaxation process could not be resolved to emphasize the generality of Eq. (4). Eq. (4) is explicitly used in the fits of the short-time behavior.

The reliability of the estimation of Γ_0 is evident in Fig. 4. The figures show the mutual dependency of the fit parameters. Clearly, the constant low- q plateau Γ_0 can be estimated independently from D_1 , n_1 which demonstrates the robustness of the fit.

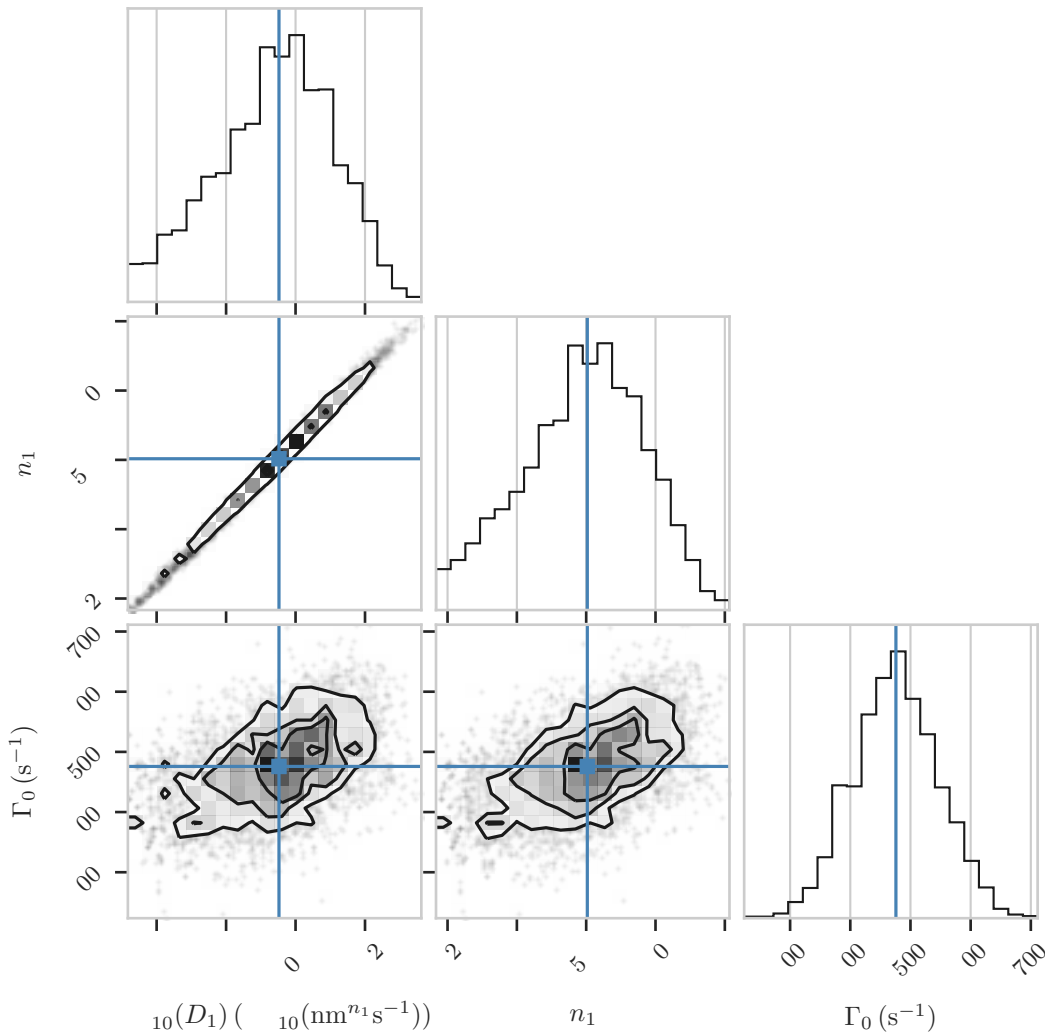


Figure 4. Posterior probability distributions (histograms) and mutual correlation plots (others) between fit parameters. The solid lines in the correlation plots indicate 25%, 50% and 75%. The blue lines indicate the maximum likelihood solution of each parameter. The fits are performed with the correlation functions shown in Fig. 2 in the letter.